Simulation of Physical Semiconductor Devices under Large and Small Signal Conditions

(Invited Paper)

B. Schmithüsen, A. Schenk*, I. Ruiz, and W. Fichtner

Integrated Systems Laboratory, Swiss Federal Institute of Technology Zurich (ETHZ), Switzerland,
*Email: schenk@iis.ee.ethz.ch, Tel: +41 1 632 66 89, Fax: +41 1 632 11 94, URL: www.iis.ee.ethz.ch .

In this paper we demonstrate the use of a physics-based device simulation approach for RF applications. We describe the modeling frame for physical semiconductor devices given by PDE-based transport model equations and illustrate the extraction of relevant technical parameters.

I. INTRODUCTION

Modern electronic systems require various levels of modeling depending on the design tasks. In the RF area, most simulations are performed on the level of compact modeling of nonlinear circuits, both by time- and, especially, frequency-domain analysis methods. For small building blocks consisting of only one or two nonlinear devices, physics-based simulation offers several advantages and possibly new insights into the device. The major advantage of such a physics-based approach is that only one model is used which is valid for the whole range of operating conditions, is independent of the applied frequencies, covers both small and large signal excitations, includes technology and material parameters, and abandons the quasi-static assumption. On the other side, this approach requires much more computer resources than compact modeling, and hence, becomes feasible only for networks where the optimization of one or two kernel devices improves the overall performance.

II. MODELING FRAME AND ANALYSIS METHODS

The employed simulation environment [1] allows the electro-thermal simulation of both SPICE-like and physical devices, i.e. so-called mixed-mode simulations. In general, the dynamic problem takes the form

$$\frac{d}{dt}q(r, x(t,r)) + f(r, D_r, x(t,r), w(t)) = 0 \,, \quad (1)$$

where x are the solution variables, D_r indicates the dependence on spatial derivatives, and w denotes explicitly time-dependent sources.

A. Physical Devices

If the transport in physical devices is described by the drift-diffusion (DD) model, (1) is given by

$$-\nabla \cdot (\epsilon \nabla \psi) = q \, (p - n + C) \,, \quad (2)$$

$$q\frac{\partial n}{\partial t} - \nabla \mathbf{j}_n = -q \, R \,, \; q\frac{\partial p}{\partial t} + \nabla \mathbf{j}_p = -q \, R \,, \quad (3)$$

and the current densities are given by

$$\mathbf{j}_n = q \, (D_n \nabla n - \mu_n n \nabla \psi) \,, \quad (4)$$

$$\mathbf{j}_p = -q \, (D_p \nabla p + \mu_p p \nabla \psi) \quad (5)$$

General: Mixed-Mode, Electro-Thermal, HSPICE models, 1D-3D Physical Devices, Compact Model Interface (CMI) Heterostructure Devices
Transport: DD, TD, HD, QDD, MC
Physical Models: Thermionic Emission, Gate Current, Schrödinger Eq., Optics, Physical Model Interface, ...
Analysis: DC, Transient, AC, Noise, Harmonic Balance

Fig. 1.   Features of the simulation platform.

(standard notations are used) on a simulation domain Ω representing an arbitrarily shaped device structure in one, two, or three space dimensions and consisting of different materials. Energy-balance (EB) or/and lattice heat equation might be included, too. The simulator takes as an input process data in form of geometrical material systems and spatially distributed doping information (generated by process simulation or by analytical expressions). An overview on simulation capabilities is given in Fig. 1.

B. DC and Transient Analysis

For numerical purposes, the transport equations are spatially discretized on a simulation grid by the stable Scharfetter-Gummel box method (a nonstandard finite-element method suitable for diffusion-convection problems) resulting in

$$\frac{d}{dt}q(r, x(t)) + f(r, x(t), w(t)) = 0 \quad (6)$$

in full analogy to the general equation of circuit simulation. However, the transients require stable implicit time-stepping methods, such as Backward Euler or TRBDF2, i.e. the solution of a nonlinear problem per time step. Just to contrast physics-based simulation to compact modeling, the number of unknowns for typical 2D simulations are in the order of several 10'000 (depending on mesh size and transport model). Fig. 7 shows the grid for the 2D structure of the bipolar transistor discussed in the next section.

C. Small-Signal Analysis

Small-signal characterizations of the system at a given DC solution x_0 are achieved assuming that sinusoidal signals $w(t) = w_0 + W_1 exp(j\omega t)$ are applied

as boundary conditions by linearizing both q and f. Fourier transformation results in the linear system $(j\omega q'(x_0) + f'(x_0)) X_1 + W = 0$. Its solution X_1, i.e. the phasors of the AC solution variables ψ, n, and p, and the AC current densities might give insights into the small-signal device operation.

D. Large Signal Analysis

In this paper we perform the large-signal analysis by transient simulations. A harmonic balance (HB) module, standard in large-signal RF circuit simulation of nonlinear systems and well suited for periodic or almost-periodic excitations, is currently under development for the mixed-mode device simulation platform (similar to the one of [2]). Though transients allow the simulation of arbitrary excitations, HB offers advantages for systems with widespread time constants of interest in terms of required computer resources.

HB assumes that all solution variables are represented by a Fourier series, i.e. given by $x(t) = X_0 + \Re\left\{\sum_{h=1}^{H} X_h exp(j\omega ht)\right\}$ in the one-tone case. The solution variables are now given by the vector of all Fourier coefficients, resulting in a nonlinear system

$$G(X) := j\Omega Q(X) + F(X) = 0 \quad . \tag{7}$$

This nonlinear system is solved with Newton like procedures, where the necessary derivatives $\frac{\partial}{\partial X} F(X)$ can be expressed by the spatial derivatives at different time points, i.e. the simulator switches between time and frequency picture. The system size grows linearly with the number H of harmonics included, whereas memory requirements increase with $O(H^2)$. By using preconditioned iterative solvers, the solution time might be kept in the order of $O(H^2)$. Hence, on device level, HB analsyis has not been of widespread use so far, as typical simulations reach or even exceed computer resources in terms of memory consumption and simulation time, but might become more practical in view of the rapidly increasing computer resources. Furthermore, convergence of simulations, a preservative problem in solving nonlinear systems, is hard to achieve for bipolar transistors with external circuitry. Part of our research is to improve the numerical HB analysis, to make it a valuable tool for physics-based large RF signal optimization tasks.

E. Noise Analysis

On the physical level noise is modeled by the direct impedance field method [3] using an efficient Green's functions approach for noise propagation [4]. Noise sources are treated as Langevin sources s for the system under investigation, i.e. the system reads $f'(x_0)\delta x = s$. Noise sources originate from local fluctuations of carrier densities and current densities spatially distributed over the device. The noise voltage

correlation spectra (for circuit nodes at r and r') result in integral expressions of the form [5]

$$S_{V,V}(r, r'; \omega) = \tag{8}$$
$$= \sum_{\alpha,\beta} \int_{\Omega} \Gamma_\alpha(r, r_1; \omega) K_{\alpha,\beta}(r_1; \omega) \Gamma_\beta^*(r', r_1; \omega) dr_1 +$$
$$+ \sum_{\alpha,\beta} \int_{X} \underline{\Gamma}_\alpha(r, r_1; \omega) \underline{\underline{K}}_{j_\alpha, j_\beta}(r_1; \omega) \underline{\Gamma}_\beta^*(r', r_1; \omega) dr_1$$

where $K_{\alpha,\beta}$ and $\underline{\underline{K}}_{j_\alpha, j_\beta}$ are spatially uncorrelated density and current noise sources for different physical processes, respectively. The terms Γ_α and $\underline{\Gamma}_\alpha$ describe the transport of the local noise sources to the nodes and depend on the transport model. They are computed with the help of linear Green's functions. For frequencies in the RF range, current noise is described by the diffusion noise source (here electrons)

$$\underline{\underline{K}}_{j_n, j_n}(r) = 4q^2 n(r) \mu_n(r) \tag{9}$$

In general, it is difficult to derive analytical noise source models.

III. ANALYSIS OF A POLY-EMITTER BIPOLAR RF TRANSISTOR

In this section we illustrate the simulation capabilities of the physics-based approach along a realistic example and discuss typical simulation problems for such structures without performing a calibration. The simulated structure is a double poly-emitter bipolar transistor of a $0.3\,\mu$m BiCMOS process depicted in Fig. 7. Geometry and doping information was taken from Ref. [6]. The key points of this technology are the use of shallow and deep trench isolations to achieve a low collector-base junction capacitance, and the use of a nonselective epitaxially grown base aiming at high $f_{\max}$ and BV_{ceo}.

A. DC Simulation

An accurate DC calibration is not only an indispensable step for precise DC simulations of the device, but also a pre-requisite to realistic AC and noise simulations. Mesh definition, modeling of the poly-emitter and oxide-silicon interfaces, and definition of the collector doping profile are some of the most critical issues. All simulations in this paper were performed with the device simulator DESSIS$_{-\text{ISE}}$ [1].

As apparent in Fig. 7, a strongly refined mesh in the emitter-base region is required to resolve the rapid variation of physical quantities (lifetimes, generation-recombination rates, densities). The vicinities of the trench oxide corners and regions along the trench walls demand even a higher mesh density, since peaks of the field strength and high current densities, respectively, can be found at these locations. The rounding of the trench oxide corners determines to a large extent the

Fig. 2. Forward Early characteristics.

Fig. 3. Power Gains over frequency for $I_c = 13\,\text{mA}$, $V_{\text{CE}} = 2\,\text{V}$.

Fig. 4. MAG (solid) and MSG (dashed) over I_C for $V_{\text{CE}} = 3\,\text{V}$.
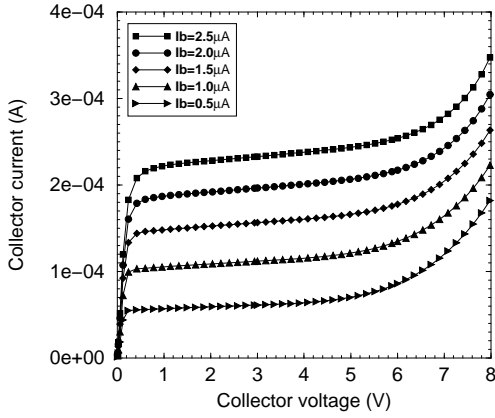
electric field around the corner and, therefore, the avalanche generation rate in the collector-base junction.

The interfacial oxide layer between poly silicon emitter and single crystalline silicon influences the transition of holes into the emitter. Because its actual form is unknown and may vary over the wafer, we chose a simple modeling approach. We used effective values for hole mobility and lifetime in the poly silicon in order to reflect and, at the same time, to simplify the description of the complex structure of the poly silicon emitter (grains, grain boundaries) and the interfacial layer between poly silicon and single crystalline silicon. The collector doping profile is crucial because of its influence on the collector current in the high-injection regime. Accordingly, the buried layer profile must be carefully modeled such that the soft-breakdown in the Early curves at high V_{CE} is best reproduced for all base currents (see Fig. 2). A stronger doping tail extending into the upper region of the collector causes an increase of the field strength and enhanced avalanche multiplication. Furthermore, the collector doping profile effects the turn-on of the saturation current in the forward Early characteristics, since a larger fraction of the collector bias can drop over the emitter-base junction at small V_{CE}.

The high-injection range is difficult to simulate because of the built-up of a strong electron-hole plasma in both base and collector. During our investigations it turned out that the resistance remained fixed by the gradient of the plasma, which fills up not only the intrinsic base, but also a large part of the collector. The density of the electron-hole plasma in the intrinsic base increases to far more than $1e19\,\text{cm}^{-3}$ and to more than $1e18\,\text{cm}^{-3}$ in the upper part of the collector. This will lead to strong carrier-induced band gap narrowing (BGN) which smears out the band gap discontinuity at the emitter-base junction and creates a gap gradient in the collector. Additionally, under high injection conditions both the impurity scattering and the electron-hole scattering are strongly screened by the plasma which makes mobility modeling a difficult task.
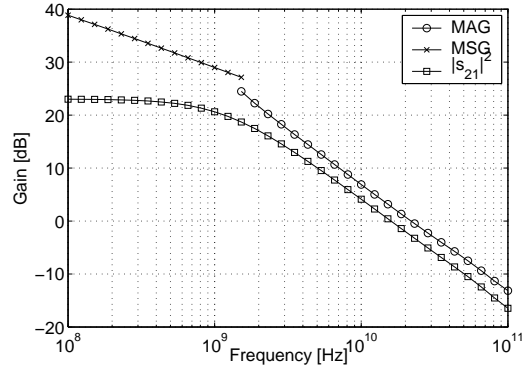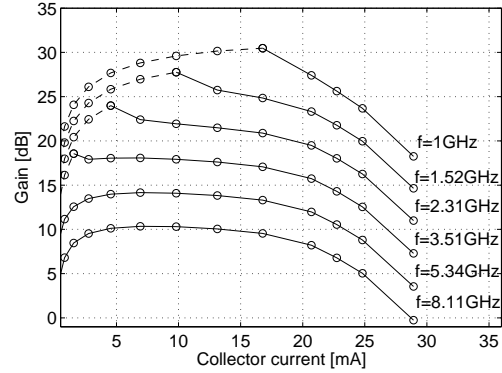
B. AC Simulations

Careful DC calibrations for realistic structures are crucial for the calibration of small-signal parameters and other higher-order effects of the device under investigation. For example, a misfit in the DC current gain will immediately be visible in poor ac parameter agreement. Further important issues are the effect of the inherently restricted simulation domain on the computed small-signal parameters, the modeling of parasitics by means of lumped elements (mixed-mode simulation), the inclusion of 3D effects, and the sensitivity on mesh definition.

The AC-analysis capabilities of DESSIS$_{-\text{ISE}}$ [1] allowed us to extract the admittance matrix of the RF-bipolar under investigation. Fig. 3 illustrates the computed maximum stable gain (MSG), maximum available gain (MAG) and unilateral two-port gain ($|s_{21}|^2$) over frequency for the DC operation point $I_C = 13\,\text{mA}$ and $V_{\text{CE}} = 2\,\text{V}$. Fig. 4 shows the dependence of the maximum stable and maximum available power gain on the collector current. Finally, Fig. 5 presents the variation of the transit frequency with the bias point. The results are satisfactory, since the computed curves correspond to the expected small-signal characteristics of such a bipolar device.

C. Large-Signal Simulations

The circuit used for the large-signal simulations consists of a 1 GHz AC voltage source with a real source
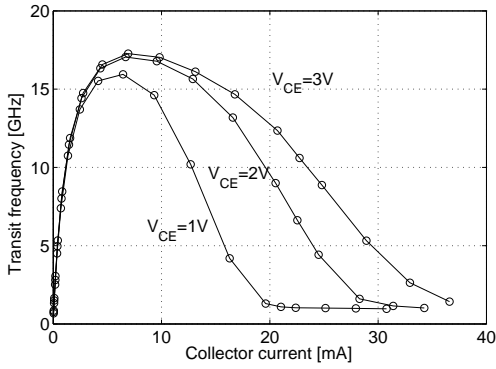
Fig. 5. Transit frequency over collector current for $V_{CE} = 3$ V.
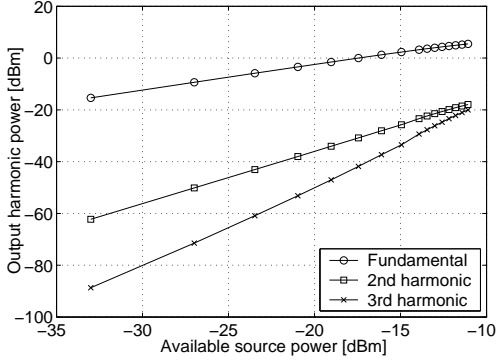
Fig. 6. Fundamental and harmonic power at $V_{CE} = 3$ V.

impedance of $Z_S = 50\,\Omega$, the active device under investigation, a real load impedance $Z_L = 50\,\Omega$ and the proper bias network. Note that the load impedance is frequency-independent, i.e. identical loading conditions apply to all signal frequency components present at the output of the device. Fig. 6 illustrates the fundamental and harmonic output power referenced to the source available power. For small excitations the harmonic power slope behaves as expected, i.e. n dB/dB for the nth harmonic. For higher input powers the curves start to deviate from the small-signal behavior as a result of the increasing influence of the system's nonlinearity. The 1-dB compression point CP_{1dB} and the third-order intercept point $IP3$ ($f_1 = 1\,$GHz, $f_2 = 1.1\,$GHz) computed for the bias point ($V_{CE} = 3$ V, $I_C = 13\,$mA are $CP_{1dB} = (-11.07, 5.46)$ dBm and $IP3 = (4.5, 22)$ dBm, respectively. From a qualitative point of view, we can afirm that the simulated large-signal behavior is consistent with the expected one. All large-signal computations were done by transient simulations, though it might be natural to use the frequency domain HB analysis here. However, for the given circuitry the HB module failed to converge. The simulation were done with an AC voltage source ramped from 0V up to the compression point of about 0.1V. The HB simulation failed to step further than 2.5 mV voltage swing, i.e. much below the compression point. In fact we observed that for such small amplitudes at the base contact, an amplitude of about 0.1V for the first harmonic of the potential can
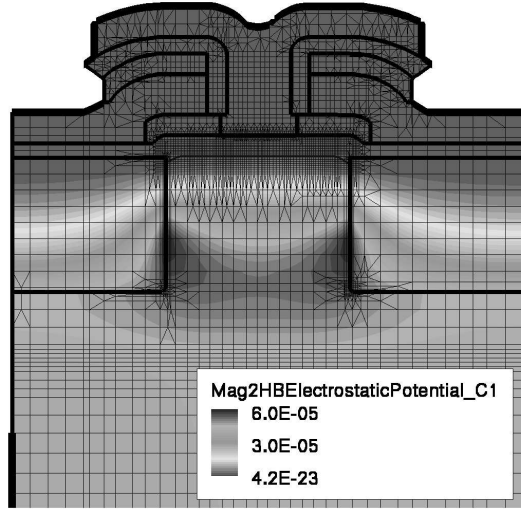
Fig. 7. Amplitude square of the fundamental of the potential.

be observed in the collector region close to the trench interfaces (Fig. 7).

IV. CONCLUSION

We demonstrated the use of a physics-based simulation environment for typical RF design and optimization tasks. The modeling frame of a mixed-mode simulation platform with PDE-based transport description for the charge carriers including its analysis capabilities has been described. It has been shown that important figures of merit can be well described by these methods. On the other hand, to bridge the gap between ECAD and TCAD RF simulations, an efficient HB module within TCAD might be of particular interest. However, physics-based RF simulations will not replace compact simulations due to the high demand for computer resources although it might be a valuable tool for the optimization of kernel nonlinear devices.

REFERENCES

[1] *DESSIS (V 9.5)*, ISE Integrated Systems Engineering AG, Switzerland, 1994-2004, (http://www.ise.ch).
[2] B. Troyanovsky, "Frequency domain algorithms for simulating large signal distortion in semiconductor devices," Ph.D. dissertation, Stanford University, 1998.
[3] W. Shockley, J. A. Copeland, and R. P. James, "The impedance field method of noise calculation in active semiconductor devices," in *Quantum Theory of Atoms, Molecules and the Solid State*, P.-O. Loewdin, Ed. Academic Press, 1966, pp. 537–563.
[4] F. Bonani, G. Ghione, M. R. Pinto, and R. K. Smith, "An efficient approach to noise analysis through multidimensional physics-based models," *IEEE Trans. Electron Devices*, vol. 45, no. 1, pp. 261–269, Jan. 1998.
[5] A. Schenk, B. Schmithüsen, A. Wettstein, A. Erlebach, S. Brugger, F. M. Bufler, T. Feudel, and W. Fichtner, "Simulation of RF noise in MOSFETs using different transport models," *IEICE Trans. Electron*, vol. E86-C, no. 3, pp. 481–489, Mar. 2003.
[6] H. Nii, C. Yoshino, S. Yoshitomi, K. Inoh, H. Furuya, H. Nakjima, H. Sugaya, H. Naruse, Y. Katsumata, and H. Iwai, "An $0.3-\mu m$ Si Epitaxial Base BiCMOS Technology with 37-GHz f_{max} and 10-V BV_{ceo} for RF Telecommunication," *IEEE Trans. Electron Devices*, vol. 46, no. 4, pp. 712–721, Apr. 1999.